Tellus (1983), *35A*, 173–188

Large-scale fluctuations in a long-range integration of the ECMWF spectral model

By JEAN PIERRE VOLMER and MICHEL DÉQUÉ, *Météorologie Nationale, 77 rue de Sévres, 92100 Boulogne, France,* and MICHEL JARRAUD, *European Centre for Medium-Range Weather Forecasts, Shinfield Park, Reading, Berkshire RG2 9AX, England*

(Manuscript received November 15, 1981; in final form October 12, 1982)

ABSTRACT

The ECMWF spectral model with a triangular T21 truncation has been integrated for a 6-year period. The chronology of the atmosphere simulated by the model is studied through Principal Component Analysis of the 500 mb geopotential field. The annual cycle is found to be predominant, but the interannual variability is shown to be large and the model proves able to generate long and persistent anomalies, even though sea-surface temperatures change only with a climatological annual variation.

1. Introduction

General Circulation Models (GCMs) have proved to be able to simulate the mean atmosphere reasonably accurately. Many experiments have been carried out by several groups, and most of them are described in the report by the JOC study conference on climate models (GARP, 1979). Nowadays, the increase in computer power has made feasible very long integrations over several years which allows an analysis of the interannual variability of a model. Such experiments have been carried out by a few groups (e.g. Schlesinger and Gates, 1979; Cubasch, 1981; Lau, 1981). Schlesinger and Gates (1979), using a 2-level model integrated over 3 years, investigated the interannual model variability by comparing the synoptic patterns of mean months (or seasons) in the various years of the integration. As an alternative to comparing synoptic patterns, a statistical approach can be used, the Principal Component Analysis (PCA), known in meteorology as Empirical Orthogonal Functions (EOF) decomposition. It was introduced in meteorology by Fukuoka (1951) and Lorenz (1956), and has been subsequently used widely either for data comparisons, or for numerical prediction by, for instance, Obukhov (1960). Holmström (1963), Fechner (1977), Rinne and Karhila (1975), to quote but a few. Such an approach was chosen by Lau (1981) to analyse the results of a 15-year integration carried out with a version of the 9-level GFDL spectral model using a rhomboidal truncation with 15 zonal wave numbers (Manabe and Hahn, 1981). The method was applied mainly to the Northern Hemisphere winter. He found that the preferred modes of oscillation in the model atmosphere had a coherent 3-dimensional structure and were characterized by wave-like patterns with multiple centres of action. The corresponding anomalies were similar to observed atmospheric standing oscillations.

In this paper, the results of a 6-year integration with the ECMWF spectral model, using a triangular T21 truncation, are analysed through successive PCAs. The main purpose is to study the time variability of the atmosphere simulated by the model, restricting ourselves to its most important features depicted by the first EOFs (which are time independent) and by the corresponding components (which are only time dependent). It does not attempt to present a detailed check of the results against reality. Such a comparison is presently under way and will be described in a forthcoming publication.

After having recalled the experimental design and the statistical method used, we make a PCA of the 6 years, showing that the annual cycle is predominant, as expected. Nevertheless, other signals can be observed. Special attention is drawn to the interannual variability and to the ability of the model to simulate realistic anomalous episodes, even in the latter stages of this long integration. We were also able to trace a senescence of the model, but this is shown to be very weak and not to affect its suitability for general circulation studies.

2. Description of the experiment

The model used is the ECMWF global 15-level spectral model with a triangular truncation T21 (i.e. up to zonal wavenumber 21) and sigma as the vertical coordinate (Baede et al., 1979). It will hereafter be referred to as "T21" only. The choice of the spectral technique was based on efficiency reasons, since at the fairly low resolutions used, spectral methods are much cheaper than equivalent finite difference methods. Furthermore, Manabe et al. (1979) reported that in many respects a spectral model with a rhomboidal 15 truncation could out-perform a grid point model of substantially higher resolution for general circulation studies, despite some difficulties in describing the precipitation field. Our choice of a triangular truncation rather than a rhomboidal one like McAvaney et al. (1979), Manabe et al. (1979) and Lau (1981) was based on experiments carried out at ECMWF (as yet unpublished), showing a clear superiority of the triangular truncation, in particular at high levels. Finally, although higher resolution extended integrations carried out at GFDL (Manabe et al., 1979) or ECMWF (Cubasch, personal communication) show an improvement in many important features (like the north–south gradient in the Southern Hemisphere), they also exhibit some stronger errors (like a more pronounced over-development of low-pressure areas in the Northern Hemisphere). Since resolutions comparable to T21 have been shown to be able to simulate the major characteristics of the general circulation reasonably correctly, and since we needed to integrate the model over several years in order to investigate the interannual variability, "T21" appeared as a good compromise between the expected quality and the cost of such an experiment. For his 15-year integration, Lau (1981) used a similar resolution (rhomboidal 15).

The model used has a horizontal diffusion of the form $-K\nabla^4$ with $K = 2 \cdot 10^{15}$ m^4 s^{-1}. The parameterization of subgrid scale processes is described in Tiedtke et al. (1979). It includes radiation, large-scale condensation, dry and moist convection, boundary layer and vertical turbulent fluxes. The zenith angle is updated before any radiation computation carried out at 12 h intervals and there is no daily cycle. The snow cover and its influence on albedo and the cloud cover are predicted. The surface roughness is specified over land and computed over sea. The surface temperatures over sea are updated every 4th day to values interpolated from monthly climatologies; over land they are predicted. Nevertheless, as a result of a coding error, the surface temperatures over frozen sea (not predicted) were not updated and the sea-ice was not allowed to melt thereafter. Moreover, the temperature and moisture in the deep soil, used for fluxes into the ground, were kept constant over land at the November climatological values. However, new experiments with these deficiencies removed (not reported here), do not significantly alter the results presented in this paper.

The starting date for the experiment was November 15, 1979. The model was then run until January 1, 1980, that is for 46 days, in order to get closer to its own climatological balance. Finally, a 6-year simulation was carried out. The results were saved every 2nd day of the integration. Detailed studies of the model climatology have been made by Cubash (1981), demonstrating the potential of T21 for general circulation studies. Therefore we shall only briefly recall the major features.

The 500 mb geopotential field for January is displayed in Fig. 1 for both the atmosphere (climatology from NCAR) and the mean T21 simulation. The main climatological troughs and ridges are simulated by T21 in approximately the correct position (except the eastern Pacific ridge which is shifted towards the east), but the amplitudes are too weak. The meridional gradients are substantially underestimated in particular in the Southern Hemisphere, as in most other low-resolution GCMs so far. In Fig. 2 we compare the seasonal variability of the 500 mb geopotential field (January minus July maps) for both the real and the model atmosphere. The T21 variability is too weak in the Northern Hemisphere, mostly over continental areas, but the main maximum and minimum areas are reasonably well captured. Fig. 3 shows latitude-pressure cross sections of zonally

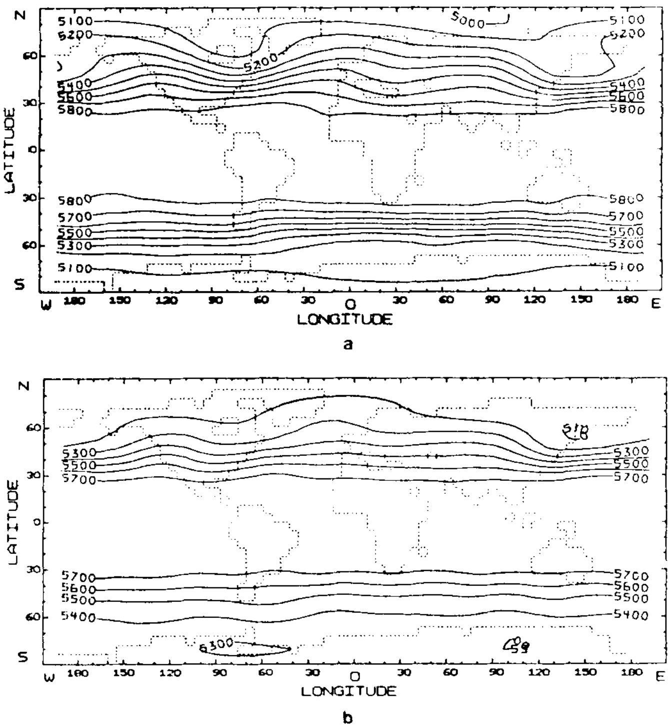

Fig. 1. Distribution of geopotential height (the contour interval is 80 gpm) at 500 mb based on time averages over 6 January months simulated by T21 (a) and on January climatology (b) obtained by NCAR from observed data.

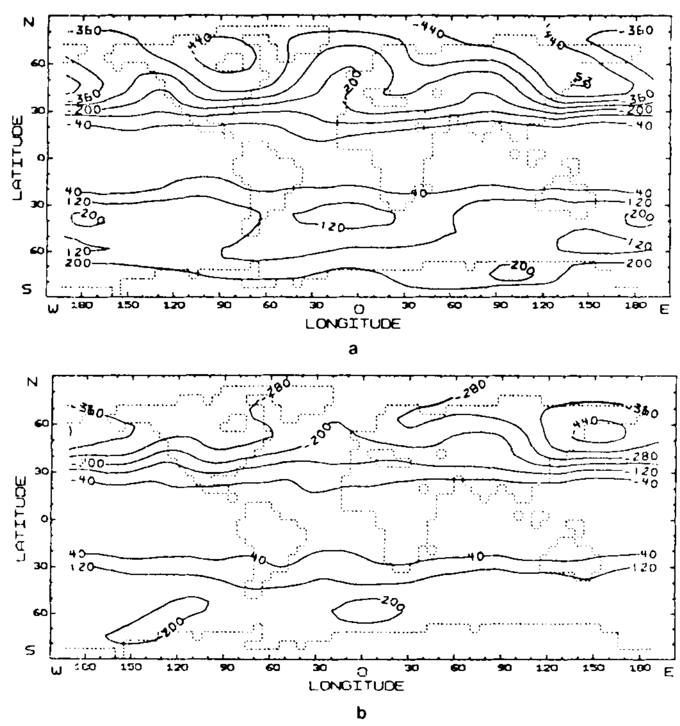

Fig. 2. As in Fig. 1 for January minus July averages.

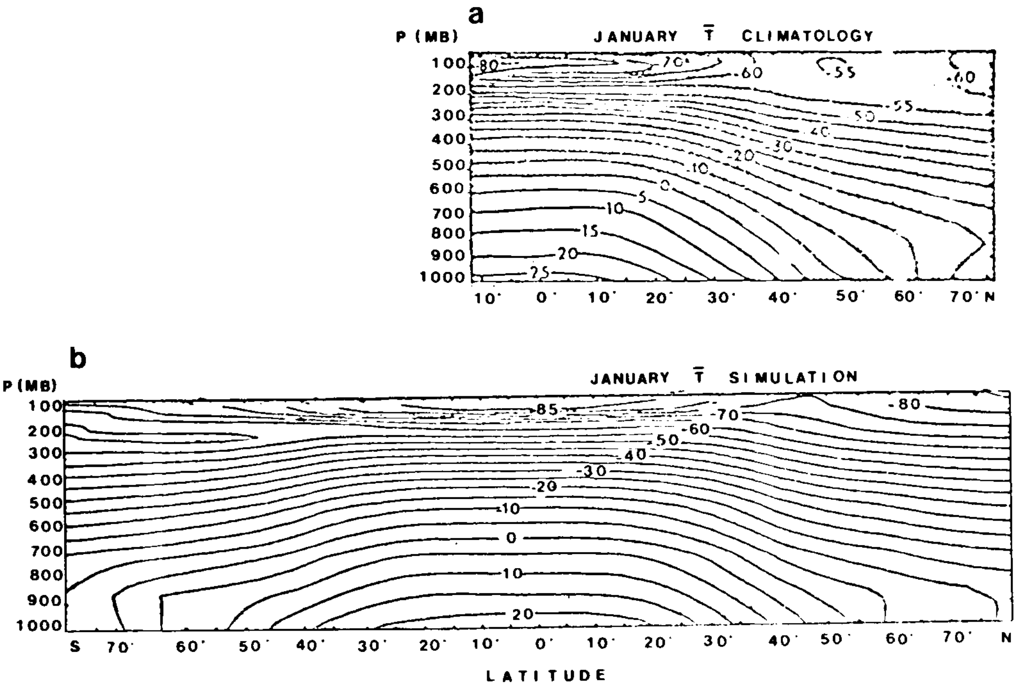

Fig. 3. Latitude-pressure cross section of zonally averaged temperature (°C) for January climatology from Oort and Rasmusson (1971) (a) and T21 simulation (b).

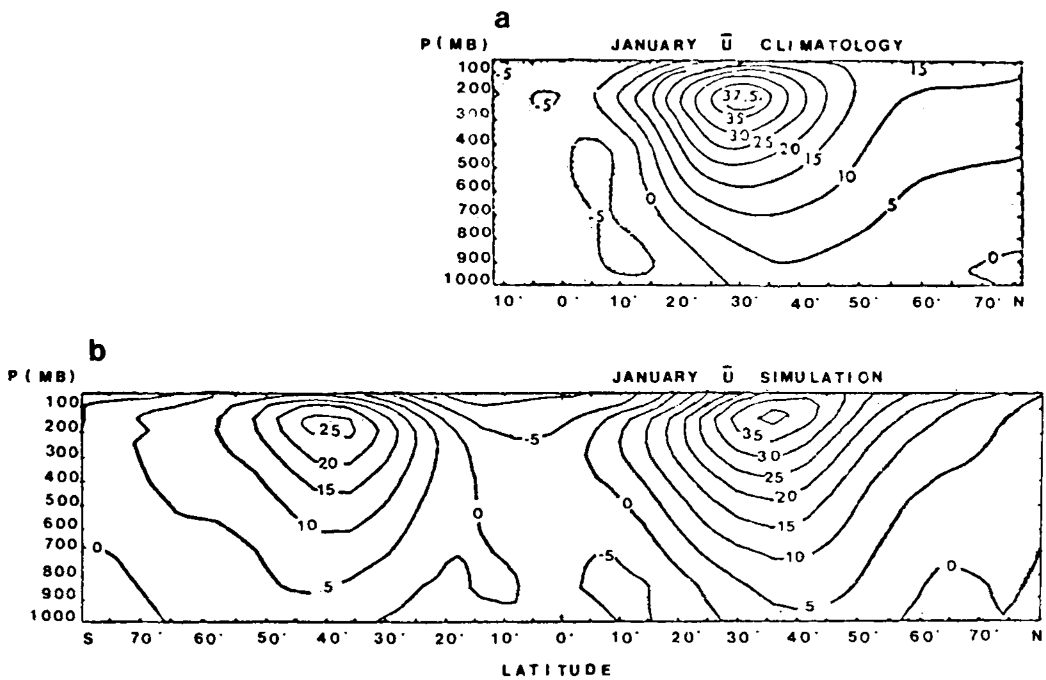

Fig. 4. As in Fig. 3 for zonal wind (m s^{-1}).

averaged temperature for the January climatology and T21 atmosphere. The model is too cold mainly in the stratosphere and in the middle troposphere. Near the surface it is too cold in the tropics but too warm near the poles. In Fig. 4 we present latitude-pressure cross sections of the zonally-averaged zonal component of the wind for the January climatology and T21 integration. The model's jet in the Northern Hemisphere is shifted towards north and is slightly too high up and too intense; however, the trade winds in the tropical belt are reasonably simulated.

3. Description of the statistical method

We will concentrate on the time evolution and main characteristics of the 500 mb geopotential field (referred to as "Z" in the following), which is a major component of the general atmospheric circulation. We had the values of Z every 2nd day of the integration (that is 1098 times), and in order to concentrate the information we decided to perform a PCA. We did it directly on the spectral components of $Z(x_i(t))$ rather than on the grid point values as done by many other authors.

If $Z_m(\lambda, \theta)$ is a proper time average of Z then

$$Z'(\lambda, \theta, t) = Z(\lambda, \theta, t) - Z_m(\lambda, \theta)$$

$$= \sum_{i \in \mathrm{T21}} x_i'(t)\, Y_i(\lambda, \theta), \qquad (1)$$

where λ = longitude, θ = latitude and Y_i = ith spherical harmonic.

The covariance matrix is thus

$$(v_{xx})_{ij} = \frac{1}{N} \sum_{k=1}^{N} (x_i'(t_k)\, x_j'(t_k)), \qquad N = 1098 \qquad (2)$$

This matrix is symmetric, positive-definite. Its eigenvalues (λ_i) can be arranged in decreasing order ($\lambda_1 > \lambda_2 > \ldots$), where λ_i is the variance derived from the corresponding eigenfunction (EOF), $C_i(\lambda, \theta)$.

$$\sum_{l=1}^{K} \lambda_l / \sum_{l=1}^{484} \lambda_l$$

is the % of variance explained by the K first EOFs. Z' can then be written

$$Z'(\lambda, \theta, t) = \sum_{i \in \mathrm{T21}} Z_i(t)\, C_i(\lambda, \theta).$$

The C_i do not depend on time. The temporal variations (the interannual variability in particular) can be investigated through the $Z_i(t)$. Practical problems arise, however, when diagonalizing the v_{xx} matrix (its order is 484 × 484). We had thus to restrict ourselves to a subset of the spectral components, namely a triangular T13 subset. (The corresponding matrix size, 196 × 196, was the maximum that could be processed with the computer available in the French Meteorological Office.) This choice is likely to have a very small impact on the actual large-scale structure of the first EOFs in which we are interested (as has been confirmed by making a control PCA on a triangular T10 subset).

This is related to the fast convergence of spectrally truncated fields towards the real field. If

$$v_i = \frac{1}{N} \sum_{k=1}^{N} (x_i'(t_k))^2,$$

then

$$\sum_{i \in \mathrm{T13}} v_i / \sum_{i \in \mathrm{T21}} v_i$$

was found close to 94%. The error made by truncating to T13 corresponds to relatively small and transient features. The long-range fluctuations of Z such as the annual cycle and the anomalies of the circulation over one or several weeks are likely to occur in the large or very large scales and we should thus be able to investigate them with this T13 analysis.

4. PCA over the 6 years

PCAs were successively performed on 2, 3, 5 and 6 years and the first EOFs were found to be extremely stable in their large-scale structure. In the PCA over 6 years, 48% of the variance was explained by C_1, then it dropped to 4% and less for the other components. Fig. 5 displays the fraction of variance explained by the first 20 components. Let $\mathrm{AC}_T(z_i)$ be the autocorrelations of z_i at a lag of T days. Then

$$\mathrm{AC}_T(z_i) = \frac{1}{N-T} \sum_{k=1}^{N-T} \frac{z_i(t)\, z_i(t+T)}{\lambda_i},$$

$$N = 1098. \qquad (3)$$

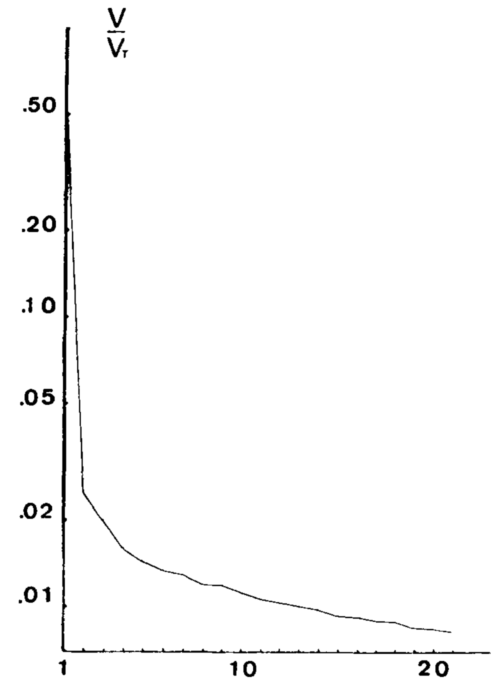

Fig. 5. Fraction of variance explained by the first 20 components (semi-logarithmic scale).

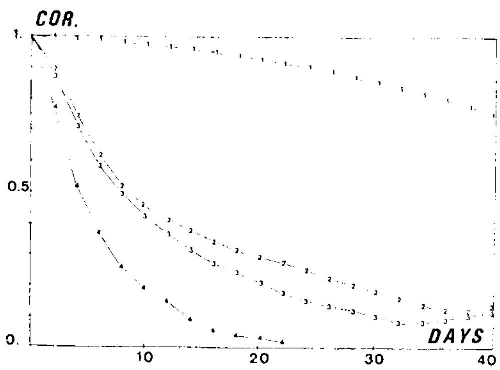

Fig. 6. Autocorrelation for lags up to 40 days. 1–1, 1st principal component; 2–2, 2nd principal component; 3–3, 3rd principal component; 4–4, 4th principal component.

Fig. 6 shows AC(z_i), $i = 1$–4 for lags of 2 to 40 days. Except for z_1 which is very persistent, the other components correspond to transient phenomena.

Fig. 7 presents the maps of C_1 and C_2 in the PCA over 6 years. C_1 shows a contrast between the Northern (NH) and Southern (SH) hemispheres. As a reference, we also display the maps of the two first EOFs obtained by Rinne et al. (1981) in a PCA over 20 years of observed data in the NH. C_1 shows a strong zonal structure in the SH. In the NH at high latitudes, the structure is more meridional. When comparing with the first EOF obtained by Rinne et al. (1981), one finds a very good agreement for all the major features, such as the intense positive maximum over the east coast of Siberia, the 2 ridges extending over Central Europe and North America, the minimum over the Norwegian sea and the trough over the east coast of the U.S.A.

It is easy to interpret this first EOF. To a first approximation, $Z = Z_m + z_1 C_1$ with Z_m increasing from the poles to the equator. So, when z_1 is strongly positive, since C_1 is positive in the NH and negative in the SH with maximum amplitudes near the poles, the north–south gradient of Z is increased in the SH and reduced in the NH. It corresponds to Austral winter. Similarly, when z_1 is strongly negative it corresponds to Boreal winter. So, C_1 reflects the annual cycle and since the trigger mechanism for it is the variation in the solar angle taken into account in the model, it is not surprising that the observed and simulated C_1 are similar in their zonal aspects. It is interesting to compare C_1 with the January minus July map (Fig. 2), which also reflects the annual cycle. It is more encouraging that the meridional structures (mainly in the NH) related to the annual cycle are also so well captured. It means that the forcings included in the model (land–sea contrast and climatologically varying sea-surface temperature in particular) are sufficient to drive them.

The second EOF (C_2) gives rise to much less variance (3%) and it is more difficult to interpret it. Fig. 7b shows that it is more symmetric with respect to the equator. It also shows 3 locations of maximum variability, one in the Northern Pacific, one in the North Atlantic and Europe and one in the SH near Australia. The two in the NH agree reasonably well with the observed ones in their large-scale structure (taking into account the different domains on which the PCA were performed), which might suggest that they are related to large-scale forcing included in the model (the land–sea contrast and the orography in particular). It is worth noting that the second EOF (corresponding to observations) is also very stable (the major features are extremely similar in the analysis over 1, 5, or 20 years).

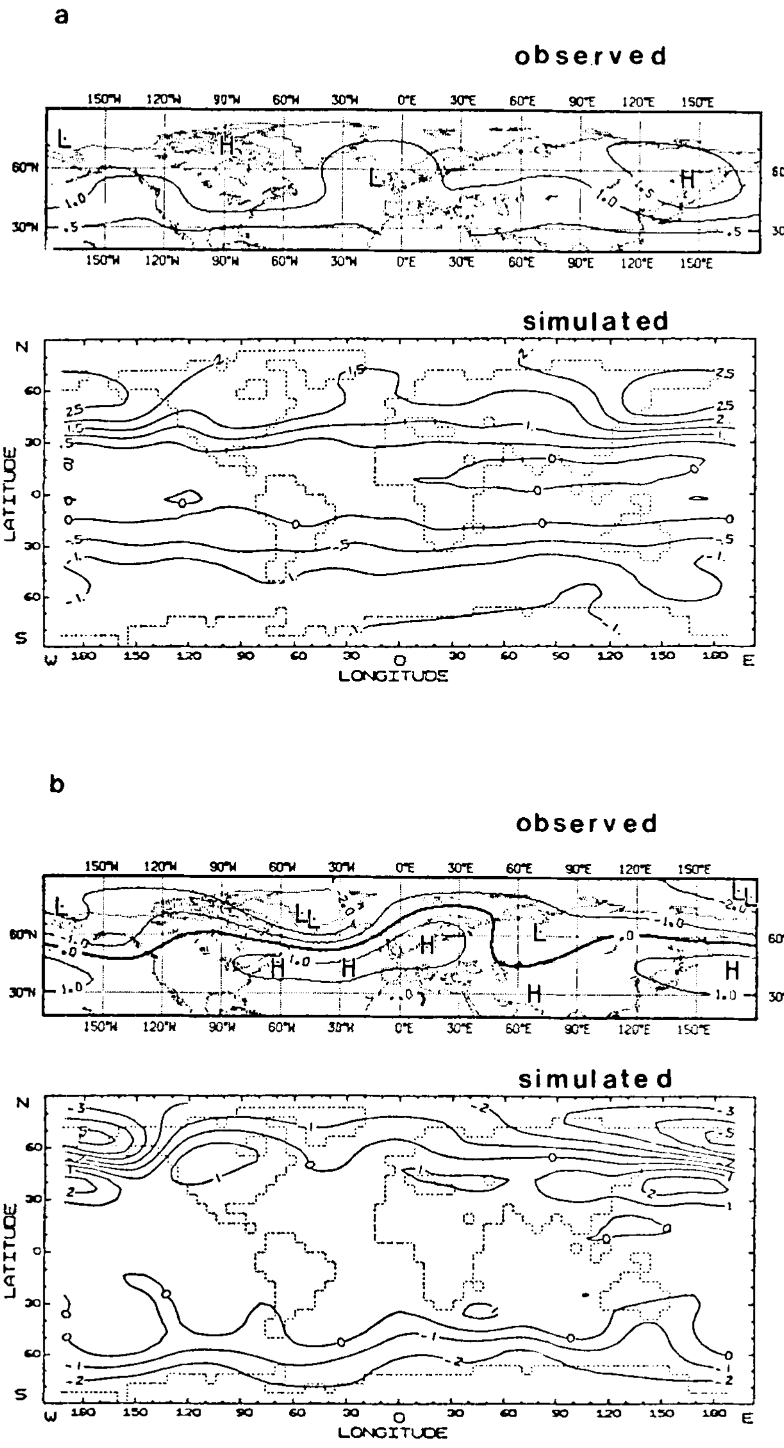

Fig. 7. Distribution of C1 (a) and C2 (b) in the PCA over 20 years of observed data in the Northern Hemisphere (from Rinne et al., 1981) and over 6 years of the T21 simulation.

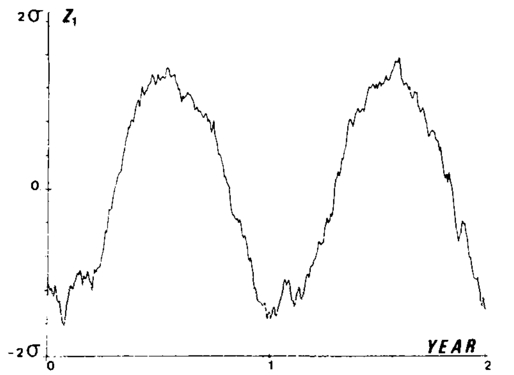

Fig. 8. Time evolution of the 1st principal component over the first 2 years (fraction of r.m.s.).

The temporal variability of Z can be investigated through the $z_i(t)$. Fig. 8 shows the time variation of z_1 over the first 2 years. It is quasi-periodic, with a period of 1 year, confirming that (C_1, z_1) portrays mostly the annual cycle. Nevertheless, some anomalous episides with a time scale of several weeks are superimposed on it. This secondary signal has an amplitude similar to that of z_3 and z_4, that gives rise to about 2% of the variance. Z_1 vanishes twice a year, once during spring and once during autumn. The first zero is very confined in time. It occurred every year between April 20 and April 26 while the second one varied between October 23 and November 10. The time evolution of z_2 is much less regular. The sign changes a dozen times a year. However, besides these very transient phenomena, z_2 shows a seasonal effect which has the same magnitude as the transient signal.

Fig. 9 shows the trajectories of different years in the (z_1, z_2) plane. Each number stands for a month and corresponds to the (z_1, z_2) value averaged over the month. The scale for z_2 is multiplied by 2 to compensate for the weakness of λ_2 compared to λ_1. The trajectories are different from year to year, but they are very well organized in the z_1 direction (reflecting the annual cycle). The interannual variability appears slightly larger in z_2 than in z_1, but some remaining seasonable aspect is clear in z_2 (especially in October and possibly near July). The strongest anomaly in z_1 is observed at the end of the 5th year and the beginning of the 6th year.

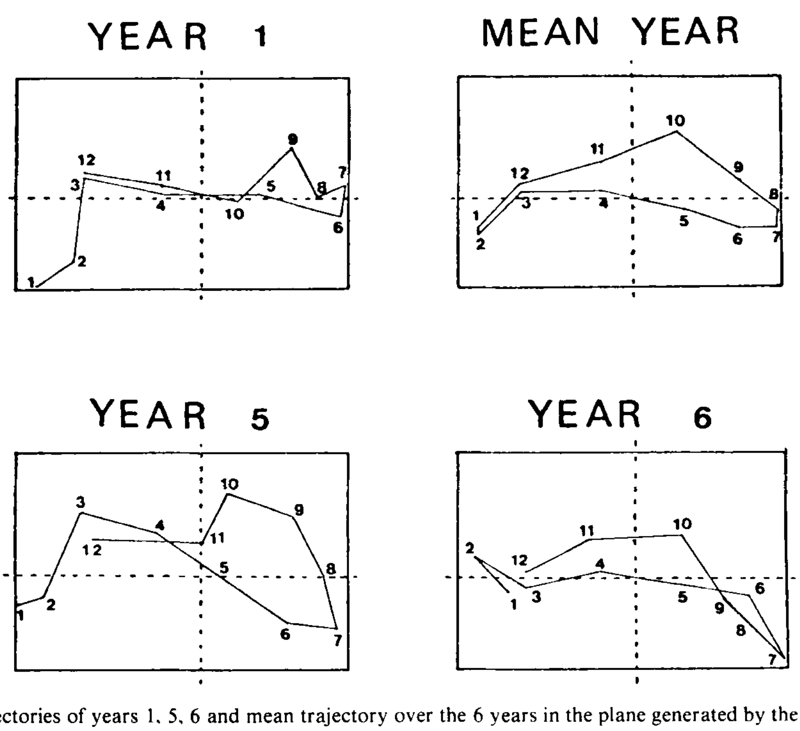

Fig. 9. Trajectories of years 1, 5, 6 and mean trajectory over the 6 years in the plane generated by the first 2 principal components. Each point stands for the mean value for the month corresponding to the number beside it (e.g. 3 = March). The ordinate (z_2 axis) has been multiplied by a factor 2.

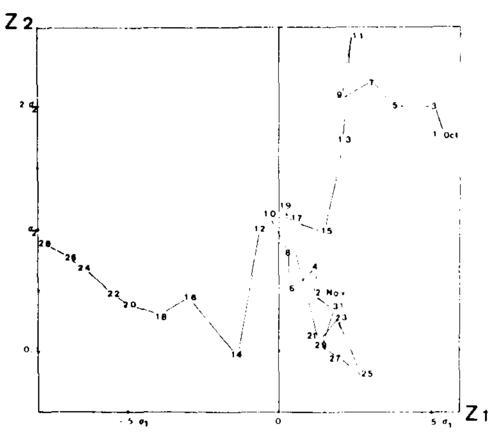

Fig. 10. Trajectory of October and November of the 5th year in the plane generated by the first 2 principal components (daily values).

November (year 5) still has a positive z_1, that is a summery character, and the following winter came very late (z_1 kept decreasing between the following January and February). Fig. 10 shows the trajectory in the (z_1, z_2) plane of October and November of the 5th year. Instead of having a smooth trend, z_1 stops decreasing near October 19 and then oscillates for more than 2 weeks before dropping again. This anomalous episode might be similar to the Indian summer which occurs in the real atmosphere. It is again worth recalling that the model is able to generate such anomalies without anomalous forcings, such as the sea-surface temperature anomalies for example. However, one should remember that these anomalies are of a similar amplitude (if not smaller) to those in the other components, z_2, z_3 and z_4. Their interpretation, in particular in the SH where the amplitude of C_1 is about half that in the NH is therefore risky.

In summary, we can say that z_1, portraying mainly the annual cycle, exhibits some non-seasonal aspects, while z_2, mostly non-seasonal, shows some seasonal features; however, the importance of the annual cycle is such that it is difficult to study the other long-range meteorological signals (i.e. with a time scale of a few weeks). Hence it is worth trying to separate the annual cycle from the other signals. The geopotential of the mean year is defined by

$$Z^M = \frac{1}{6}\sum_{i=1}^{6} Z^i,$$

where Z^i corresponds to Z in the ith year. If we perform a PCA on Z^M, C_1 accounts for 87% of the variance. The map of C_1 (not shown) is very similar to that of the C_1 discussed previously in this section, but the time evolution of z_1 is now an almost perfect sinusoid. Its phase shift compared to the solar cycle is about 1 month (the same as that observed). The other components account for only a very small amount of variance, 2% or less.

5. PCA after subtracting the mean year

Since most of the annual cycle is concentrated in the mean year, we are in a better position to investigate different signals if performing a PCA on $Z' = Z - Z^M$.

As one would expect, the information is less confined in the first components: 4.5% for C_1 and C_2, 3% and less for the others. (See Appendix A for the separation between C_1 and C_2.) When the PCA is carried out on values averaged over 10 days, the first EOFs are remarkably stable, but the variances explained increase (they become 8% for C_1 and C_2). This is not surprising since the first EOFs correspond to large-scale features in both time and space. Similar results were described in Lau (1981). The other EOFs correspond to more transient phenomena, modified by the time-averaging process which also reduces their relative importance. It also justifies our decision to concentrate on C_1 and C_2 to investigate the most important long-range fluctuations of the model atmosphere.

Fig. 11 shows the autocorrelations of the two first components (z_1' and z_2') at different lags. They are fairly persistent, since AC(z_1') drops to under 0.5 after 3 days and AC(z_2') after 5 days. The 3rd curve corresponds to the linear combinations of the first 20 components having the maximum autocorrelation at each lag. This curve decreases regularly up to a lag of 20 days. Beyond, the 0.4 level of autocorrelation is no longer reached. It means that no significant temporal wave (at least of a period longer than 20 days) is present in the model atmosphere. Fig. 12 shows the maps of the two first EOFs, C_1 and C_2. The main point is that C_1 has most of its variability in the SH and C_2 in the NH.

To a first approximation, anomalous episodes occurring in the SH can be described by $Z = Z^M + z_1'C_1$. Analogously, $Z = Z^M + z_2'C_2$ can be

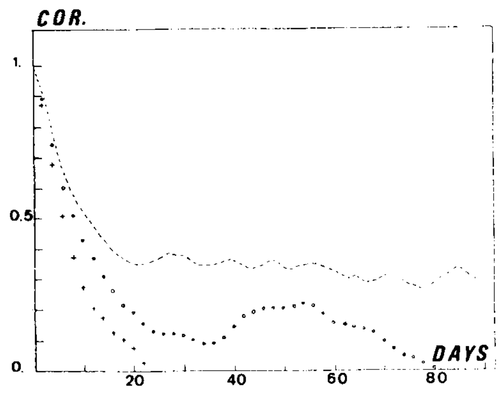

Fig. 11. Autocorrelation for lags of 2 to 90 days (PCA after subtracting the mean year). ooo, 1st principal component; + + +, 2nd principal component; — — —, maximum autocorrelation (i.e. corresponding at each lag to the linear combination of the 20 first components having the maximum autocorrelation).

used for the NH. When looking at Fig. 11, we see that these anomalous episodes appear to be slightly more persistant in the SH than in the NH. C_1 and C_2 have a very strong zonal structure in the SH and the NH, respectively (C_1 even more than C_2). Hence they can be interpreted in terms of situations with stronger or weaker north–south gradients than usual at the considered time of the year. In the NH, however, a meridional structure is observed over the Northern Pacific. Anomalies in the geopotential over north eastern America are often related to opposite anomalies over north eastern Siberia. When performing the PCA on $Z - Z^M$, we eliminated the influence of the annual cycle from the mean, but not from higher order moments. For example, the variance of z_1' during the Austral winter is twice as large as during the Austral summer. Hence we wanted to see whether anomalies were more persistent in some seasons, and in order to do that we computed the auto-

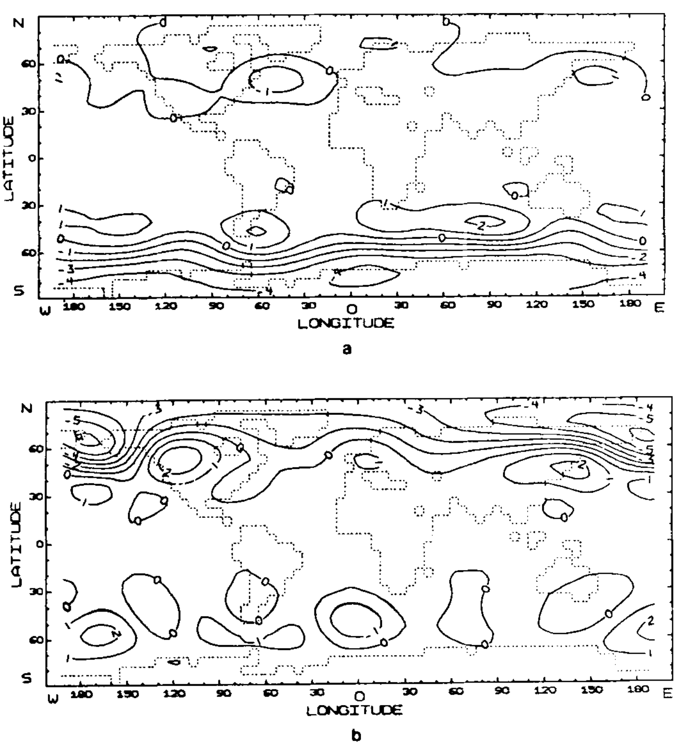

Fig. 12. Distribution of C1 (a) and C2 (b) in the PCA over 6 years after subtracting the mean year.

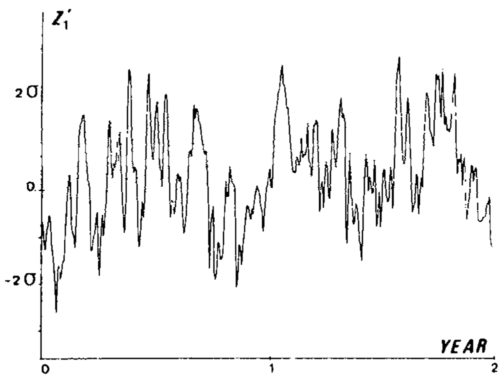

Fig. 13. Time evolution of the 1st principal component (in the PCA over 6 years after subtracting the mean year) over the first 2 years (fraction of r.m.s.).

Fig. 15. Time evolution of the 1st principal component from December 8 (year 5) to March 8 (year 6) (fraction of r.m.s.).

correlations of z_1' and z_2' at a lag of 6 days for the 6 Januaries, then Februaries. This series did not show any trend, which means that the study and comparison of anomalies over the whole year is meaningful.

Fig. 13 shows the time evolution of $z_1'(t)$ during the first 2 years. Strong anomalies lasting several weeks are observed. This tendency to produce such anomalies does not increase in the following years. In addition, the histograms of Fig. 14 display the number of episodes when z_1' (z_2') maintained a constant sign for given categories of time length.

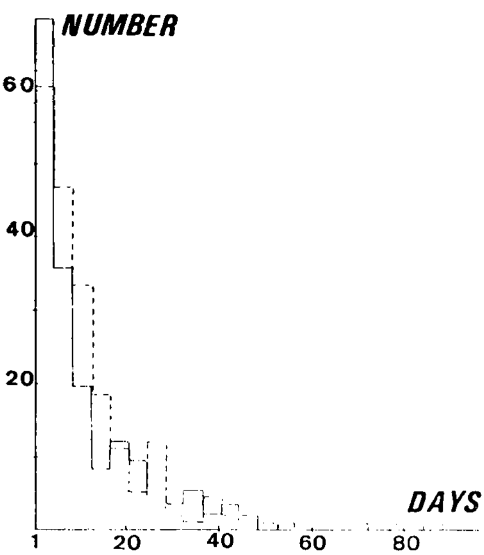

Fig. 14. Number of episodes when the two 1st principal components maintained a constant sign for given intervals of time length. The continuous (full) line shows the 1st principal component and the dashed line the 2nd principal component.

The longest anomaly (and also the strongest, reaching $3\sqrt{\lambda_1}$) in z_1' is observed in the winter between the 5th and 6th year. Fig. 15 shows the chronology of z_1' during the 86 days when it remained positive. This anomaly in z_1' is easy to interpret when looking at Fig. 11. It is concentrated in the SH with higher geopotential than usual for the season in the mid-latitudes and lower in the high latitudes. As a consequence, the north–south gradient is too strong for the season. This is clearly illustrated in Fig. 16, which shows the 500 mb geopotential map in the SH corresponding to the peak of the anomalous episode (December 31), which can be compared to a "normal" map for the season (January 1 of year 2).

This very long anomalous period in the SH bears no resemblance at all to a "blocked" situation. On the contrary, the circulation is much stronger (more wintery) than usual for SH summer. In the NH, the effects of a simultaneous anomaly in the second component were extremely different. As noted previously, the pattern of C_2 is more meridional than that of C_1, in particular over the Northern Pacific and Atlantic oceans. In order to best show the different natures of NH and SH anomalous episodes, we present in Fig. 17 the map corresponding to a peak (January 27) of a strong anomaly in z_2' when z_2' remained smaller than $-3\sqrt{\lambda_2}$ for more than 7 days (from January 23 to January 29 in year 3). In order to help interpret this map, Fig. 17 also shows the mean model forecast for January (i.e. the model's climate). Over the Pacific the highly meridional structure of the anomalous flow is clear. A very intense ridge

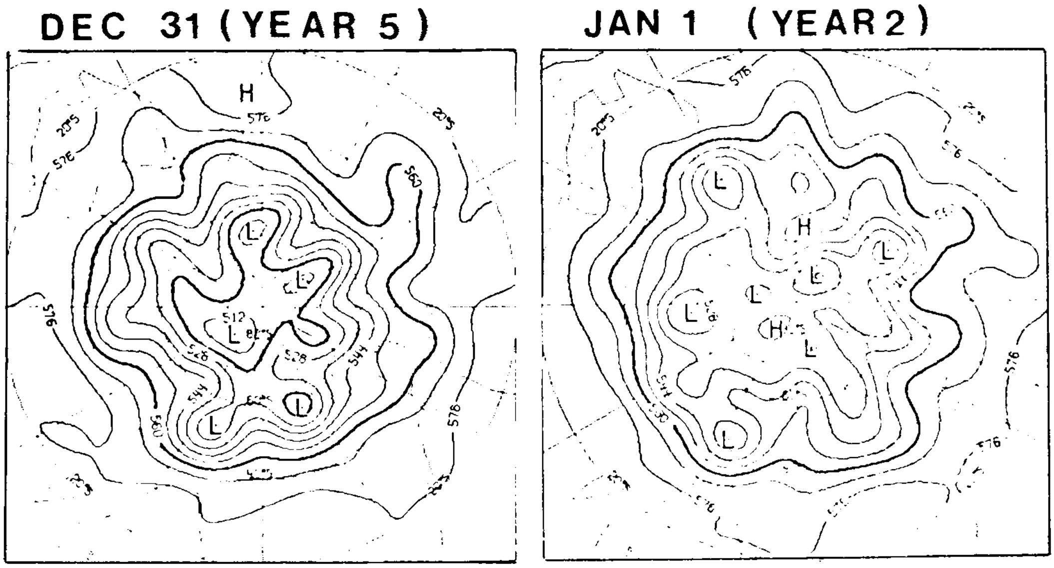

Fig. 16. 500 mb geopotential maps in the Southern Hemisphere (contour interval 8 dam) corresponding to the peak of the longest z_1' anomalous episodes—December 31 (year 5)—and to a "normal" episode—January 1 (year 2).

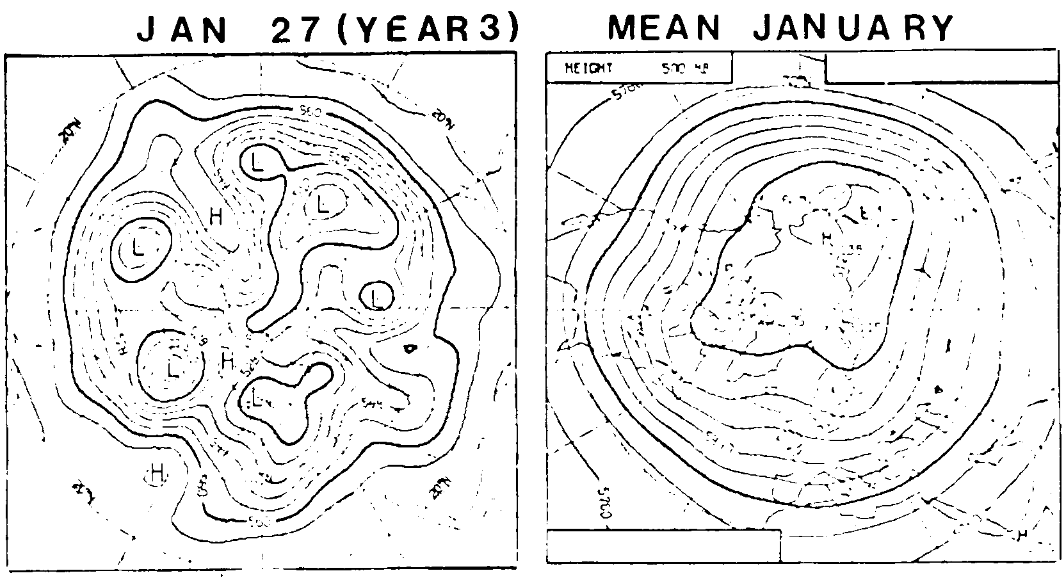

Fig. 17. 500 mb geopotential maps in the Northern Hemisphere (contour interval 8 dam) corresponding to the peak of a strong z_2' anomalous episode—January 27 (year 3) and to the January model's "climate".

blocking any westerly circulation in this region stayed there for more than a week. Looking back to the map of C_2 (Fig. 12), it corresponds to the strong negative minimum and associated trough in this region. The ridge is intensified by the presence of the 2 positive maxima of C_2 over Japan and northwestern America. (The trough over Japan in the model's climate has developed into a deep low.)

In summary, we can say that there was no coupling between NH and SH. Furthermore, the

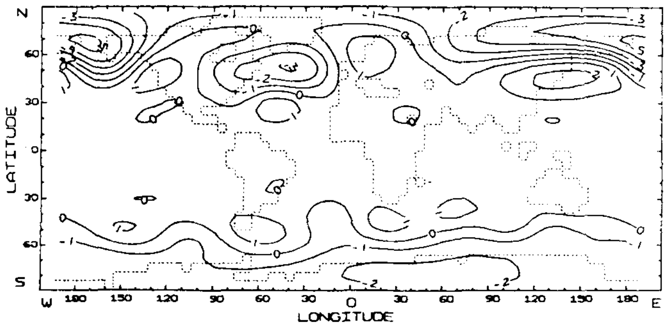

Fig. 18. Distribution of the first EOF (C1) of the PCA over the 6 winters (January + February months).

interannual variability has a very different structure in both hemispheres. In the SH, it mainly consists of a reinforcement or a weakening of the zonal flow, while in the NH it has a stronger meridional structure and anomalous episodes correspond to more stationary features.

Finally, we perform a PCA on the 12 January and February months after having removed the annual cycle. The first component, which explains 8% of variance, has an autocorrelation greater than 0.5 for 7 days. Fig. 18 displays the corresponding map. Most of the variability takes place in the NH. We can see some non-zonal effects occurring simultaneously over the North Atlantic Ocean and the East of Asia. This can be interpreted in terms of teleconnection patterns (Wallace and Gutzler, 1981).

6. Analysis of the senescence of the model

Let us again consider

$$Z(t) = \sum_{i \in T13} x_i(t)\, Y_i.$$

The x_i are known at time intervals of 2 days. Let Z^1, Z^2, Z^3 be the values of Z at 3 consecutive time intervals. A distance between Z^1 and Z^2 can be defined as

$$d(Z^1, Z^2) = \sqrt{\sum_{i \in T13} (x_i^1 - x_i^2)^2}, \tag{4}$$

where x_i^1 corresponds to Z^1 and x_i^2 to Z^2. Similarly an angle in the 196 dimensional space between (z^1, z^2) and (Z^2, Z^3) can be defined by

$$\cos(Z^1, Z^2, Z^3) = \frac{\sum_{i \in T13} (x_i^2 - x_i^1)(x_i^3 - x_i^2)}{d(Z^1, Z^2)\, d(Z^2, Z^3)}. \tag{5}$$

The products of complex numbers are to be understood as scalar products in the complex plane. It can be shown that for a phase space with the number of degrees of freedom sufficiently large (such as 196), the values of $\cos(Z^1, Z^2, Z^3)$ are usually negative. Table 1 gives the mean distances and cosines between consecutive Z, averaged over

Table 1. *Mean distances and cosines for each year*

	Year					
	1	2	3	4	5	6
Distance	106	107	106	107	105	107
Cosine (T13)	−0.204	−0.207	−0.217	−0.220	−0.220	−0.230
Cosine (0–3)	−0.095	−0.101	−0.116	−0.119	−0.130	−0.131
Cosine (4–13)	−0.303	−0.299	−0.311	−0.313	−0.303	−0.316

each year. For the cosine we also give the results for the 2 zonal wavenumber bands 0–3 and 4–13.

No trend appears in the distances, but a slight one is observed in the cosines, especially in the long waves. If computed for the mean year and averaged over successive periods of 2 months, the cosine varies between −0.208 and −0.226. This gives an estimate of its statistical annual variability. Therefore the trend observed between years 1 and 6 is likely to be significant, although it remains small. A simulation with a "random" sample (see Appendix B) resulted in a distance of 243 and a mean cosine of −0.470. This senescence corresponds to a weak change in the day-to-day variability of the model. However, its small amplitude makes any synoptic interpretation extremely difficult.

7. Summary and concluding remarks

The first PCA performed on the 500 mb geopotential field of a 6-year integration with a T21 spectral model showed that, as in reality, the annual cycle was the major feature of the low-frequency variability of the model atmosphere. The first EOF concentrating on most of this cycle thus explains the large amount of variance (40%). Beside it, a very important interannual variability, associated with the 2 first EOFs can also be observed. The map of C_1, which mostly portrays the annual cycle, shows a strong asymmetry between Northern and Southern Hemispheres. In particular there is a maximum of variability in the Northern Hemisphere near the eastern coast of Asia, while the pattern is much more zonal in the Southern Hemisphere.

When performing a PCA on the 6 years, after having removed the mean year (in order to investigate signals other than the annual cycle), we found no coupling between the 2 hemispheres. The first EOF mostly describes fluctuations in the Southern Hemisphere and the second EOF fluctuations in the Northern Hemisphere. We again found a maximum of variability over the eastern coast of Asia. In connection with this asymmetry, strong anomalous episodes were shown to correspond to more stationary patterns in the Northern Hemisphere.

In a recent paper, Wallace and Gutzler (1981) analysed teleconnections in the geopotential field during Boreal winter and asked the question: "Do similar teleconnection patterns exist in other seasons, or in the Southern Hemisphere? Do they exist in the climates generated by GCMs?" In this paper we do not give any insight for the real atmosphere, but for GCMs we could observe teleconnection patterns suggesting a positive answer to one of these questions.

As mentioned in the introduction, this paper did not aim at comparing the model's atmosphere with the real one. This will be the subject of another study. However, the features found so far at first sight do not conflict with well-known features, e.g. the asymmetries between spring and autumn, and between Northern and Southern Hemisphere variability.

In conclusion, we wish to point out that although we had fixed boundary conditions (similar from year to year), the model proved quite able to simulate anomalous years, and although we could bring into evidence a weak senescence of the model, it maintained a large interannual variability during the 6 years of the integration. Thus it does not seem necessary to use variations of external forcings to explain significant changes to the general circulation and therefore, sensitivity studies made with GCMs should be done on large samples in order to attain statistical significance. Moreover, the ability of the model to generate large and persistent anomalies may have some influence on long-range predictability.

8. Acknowledgements

Special thanks are due to U. Cubasch, whose contribution in running the experiments was decisive and to A. Simmons for helpful discussions and constructive comments. We are grateful to L. Bengtsson, J. Lepas and D. Rousseau for their encouragement and continuous support. We also had stimulating discussions with J.-F. Geleyn, J. P. Labarthe and J.-F. Royer.

9. Appendix A

Separation between C_1 *and* C_2 *in the PCA done after subtraction of the mean year*

In the analysis, the explained variance was 4.48% for C_1, 4.14% for C_2 and 3.20% for C_3. Using Anderson's test (Morrisson, 1967) we get separation coefficients of 1.71 between λ_1 and λ_2 and of 18.14 between λ_2 and λ_3. Since the significance level at 95% is 5.99, λ_1 and λ_2 are degenerate. If z_1 and z_2 are the two principal components given by our diagonalization program, any couple Z_1, Z_2 with $Z_1 = z_1 \cos\alpha + z_2 \sin\alpha$, and $Z_2 = z_1 \sin\alpha - z_2 \cos\alpha$ has the same properties of uncorrelation and maximization of the explained variance. The z_1 and z_2 obtained were not independent. The correlation of $z_1(t)$ with $z_2(t+\tau)$ (referred to as $\pi_{12}(\tau)$) was increasing with time and the maps of C_1 and C_2 had the same structure in the Southern Hemisphere and the opposite structure in the Northern Hemisphere. The correlation of $Z_1(t)$ with $Z_2(t+\tau)$ is

$$\frac{\rho_{11}(\tau) + \rho_{22}(\tau)}{2} \cos 2\alpha,$$

Z_1 and Z_2 became independent for $\alpha = \frac{1}{4}\pi$. We thus took

$$Z_1 = \frac{z_1 + z_2}{\sqrt{2}} \quad \text{and} \quad Z_2 = \frac{z_1 - z_2}{\sqrt{2}}.$$

10. Appendix B

Definition of the "random" sample for approximating the mean cosine

If $\{x_i(t), i = 1, 196\}$ are the spectral coefficients of Z, then for each of them we can compute the time average $\bar{x}_i$ and a standard deviation from this average σ_i. We then create new functions $e_i(t)$ such that the probability law for all the $e_i(t)$ in the interval $[-1.5, +1.5]$ is uniform. The "random" sample is thus defined with the new spectral coefficients

$$x_i^*(t) = \bar{x}_i + \sigma_i e_i(t).$$

Thus they have the same time average and variance. Furthermore, any of the maps of $Z^*(=\sum_{i=1}^{196} x_i^* Y_i)$ would look "reasonable", but their time sequence, of course, would not.

REFERENCES

Baede, A., Jarraud, M. and Cubasch, U. 1979. Adiabatic formulation and organization of ECMWF's spectral model. ECMWF Technical Report No. 15.

Cubasch, U. 1981. Preliminary assessment of long-range integrations performed with the ECMWF global model. ECMWF Technical Memorandum No. 28. (Available from ECMWF, Shinfield Park, Reading, Berks, RG2 9AX, England.)

Fechner, H. 1977. Presentation of weather situations above a certain geographical point and for the whole hemisphere by empirical orthogonal functions. ECMWF Workshop on the use of empirical orthogonal functions in Meteorology. (Proceedings available from ECMWF, Shinfield Park, Reading, Berks., RG6 9AX, England.)

Fukuoka, A. 1951. A study on 10 days forecasts (A synthetic report). *Geophys. Mag. 22*, 177–208.

GARP 1979. Report of the JOC Study Conference on climate models: performance, intercomparison and sensitivity studies. GARP Publication Series No. 22. WMO/ICSU, Geneva, Switzerland.

Holmström, I. 1963. On a method for parametric representation of the state of the atmosphere. *Tellus 15*, 127–149.

Lau, N.-C. 1981. A diagnostic study of recurrent meteorological anomalies appearing in a 15-year simulation with a GFDL general circulation model. *Mon. Wea. Rev. 109*, 2287–2311.

Lorenz, E. N. 1956. Empirical orthogonal functions and statistical weather prediction. Scientific report No. 1. Dept. of Meteorology, Massachusetts Institute of Technology, Cambridge, Massachusetts, U.S.A.

MacAvaney, B., Bourke, W. and Puri, K. 1979. A simulation of the January global circulation using a spectral model. GARP Publication Series No. 22, WMO/ICSU, Geneva, Switzerland.

Manabe, S., Hahn, D. G. and Holloway, J. L., Jr. 1979. Climate simulations with GFDL spectral models of the atmosphere: effect of spectral truncation. GARP Publication Series No. 22, WMO/ICSU, Geneva, Switzerland.

Manabe, S. and Hahn, D. G. 1981. Simulation of atmospheric variability. *Mon. Wea. Rev. 109*, 2260–2286.

Morrisson, D. F. 1967. *Multivariate statistical methods.* McGraw Hill Book Company.

Obukhov, A. M. 1960. On statistically orthogonal expansions in empirical functions. *Izvest. Geophys. Ser. Engl. Transl.* 288–291.

Oort, A. H. and Rasmusson, E. R. 1971. Atmospheric circulation statistics. NOAA, Prof. pap. 5, US Dept. of Commerce/NOAA, Rockville, MD., 323 pp.

Rinne, J. and Karhila, V. 1975. Spectral barotropic model in empirical orthogonal functions. *Q. J. R. Meteorol. Soc. 101*, 365–382.

Rinne, J. Karhila, V. and Järvenoja, S. 1981. The EOFs of the 500 mb height in the extra tropics of the

Northern Hemisphere. Report No. 17. Dept. of Meteorology, University of Helsinki, Finland.
Schlesinger, M. E. and Gates, W. L. 1979. Performance of the Oregon State University two-level atmospheric general circulation model. GARP Publ. Ser. No. 22, WMO/ICSU, Geneva, Switzerland.
Tiedtke, M., Geleyn, J.-F., Hollingsworth, A. and Louis, J.-F. 1979. ECMWF model parameterization of subgrid scale processes. ECMWF Technical Report No. 10, 46 pp. (Available from ECMWF, Shinfield Park, Reading, Berks., RG2 9AX, England).
Wallace, J. M. and Gutzler, D. S. 1981. Teleconnections in the geopotential height field during the Northern Hemisphere Winter. *Mon. Wea. Rev. 109*, 784–812.